Observational assessment of Arctic Ocean sea ice motion, export, and thickness in CMIP3 climate simulations

R. Kwok[1]

Received 27 January 2011; revised 27 May 2011; accepted 8 July 2011; published 24 September 2011.

[1] We compare the CMIP3 model fields with observations of sea ice motion, export, extent, and thickness and analyze fields of sea level pressure and geostrophic wind of the Arctic Ocean. These variables play important roles in the distribution and annual balance of sea ice volume within the basin. While it is not expected that uninitialized simulations agree completely with observations, these assessments serve to summarize ensemble behavior, as baselines for measuring improvements, and to evaluate reliability of CMIP3 simulations (and potentially CMIP5) for projection of decline rates of Arctic sea ice coverage. We find the model-data differences and intermodel scatter in summarizing statistics are large. In a majority of model fields the mean high-pressure pattern in the southern Beaufort is significantly displaced toward the central Arctic Basin, leading to difficulties in reproducing the mean spatial patterns of sea ice circulation, thickness, and ice export. Thus, even though the CMIP3 multimodel data set agrees that increased greenhouse gas concentrations will result in reductions of Arctic sea ice area and volume, these comparisons suggest considerable uncertainties in the projected rates of sea ice decline.

Citation: Kwok, R. (2011), Observational assessment of Arctic Ocean sea ice motion, export, and thickness in CMIP3 climate simulations, *J. Geophys. Res.*, *116*, C00D05, doi:10.1029/2011JC007004.

1. Introduction

[2] Between 1979 and 2010, the Arctic sea ice extent at the end of the melt season in September has been declining at an astonishing rate of 11.5%/decade. Consequently, there is increased interest in the projections of sea ice conditions in the 21st century as reduced summer ice coverage has near- and far-field climate and ecosystems impact, as well as socioeconomic and geopolitical implications [*Hassol*, 2004].

[3] While global climate models (CMIP3 multimodel data set) agree that increased greenhouse gas (GHG) concentrations will result in a reduction of Arctic sea ice area and volume, there is much uncertainty in the projected rates at which this will occur. In particular, *Zhang and Walsh* [2006] noted that even though the CMIP3 models capture the negative trend in sea ice area, the intermodel scatter is large. Further, *Stroeve et al.* [2007] show that few models exhibit negative trends that are comparable to observations, and that the models (as a group) likely underestimate the impact of GHG loading. After examining the differences in downwelling longwave radiation associated with errors in simulated cloud coverage, *Eisenman et al.* [2007] conclude that the results of current CMIP3 models cannot be relied upon for credible projections of sea ice behavior. In a recent study, *Holland et al.* [2010] found that the large intermodel scatter in contemporary mass budgets is strongly related to variations in absorbed solar radiation, due in large part to differences in the surface albedo simulation. Notwithstanding, *Wang and Overland* [2009] used a selected subset of CMIP3 models to predict a nearly ice-free Arctic in September by the year 2037. Each of these analyses has examined different components of the model output and their contribution to model scatter. Going forward, these types of detailed assessments are useful for not only understanding the confidence that could be placed in the projected rates of changes, but they also contribute to documenting the shortcomings of individual models and perhaps suggest paths to improvements.

[4] Our present note adds to the above assessments by examining the simulated sea ice motion, export, extent, and thickness, and sea level pressure of the Arctic Ocean in CMIP3 model output, with anticipation that this type of analysis would be useful for assessment of the upcoming CMIP5 model fields. Ice motion, largely wind-driven, plays an important role in the regional redistribution, the spatial pattern of ice thickness, and the export of Arctic sea ice volume. The large-scale ice circulation within the Arctic Basin determines the advective balance of sea ice. Even though highly variable at short (daily) time scales, it is dominated on average by a clockwise pattern (Beaufort Gyre) in the western Arctic and by a persistent Transpolar Drift Stream (TDS) that exports ~10% of the area of the Arctic Basin through the Fram Strait every year. The survivability of an ice parcel within the Arctic Ocean depends on its location, residence time and thickness. The spatial distribution of Arctic sea ice thickness, with thicker ice off

[1]Jet Propulsion Laboratory, California Institute of Technology, Pasadena, California, USA.

Copyright 2011 by the American Geophysical Union.
0148-0227/11/2011JC007004

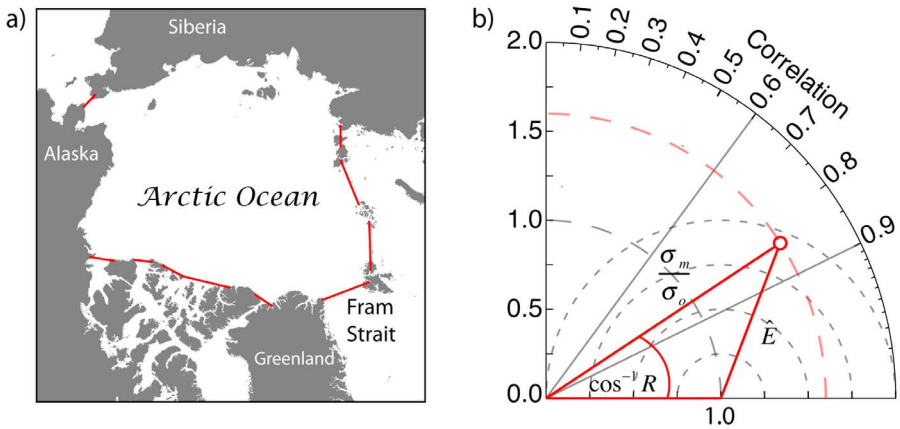

Figure 1. (a) Boundaries (in red) that define our Arctic Ocean domain. (b) Sample point (red circle) on a Taylor diagram summarizes the geometric relationship between the pattern statistics (correlation coefficient (R), the normalized RMS difference ($\hat{E}$), and the standard deviations (σ_o, σ_m)) of the model and reference fields (see description in text).

the north margins of Greenland and Ellesmere Island than the Siberian Arctic, is a feature of the ice cover that can be found in the submarine ice draft record since the 1950s and now in satellite retrievals. Therefore, if the projected ice decline rates are to be credible, the CMIP3 model fields should be able to reproduce some aspects of these features. Here, we first describe the data set and the approach used in our assessment, followed by discussions of the results, and the conclusions.

2. Data Description

2.1. CMIP3 Data Set

[5] Fields of Arctic Ocean sea ice motion, concentration, and thickness, and sea level pressure are from 17 coupled global models in the World Climate Research Programme's (WCRP's) Coupled Model Intercomparison Project phase 3 (CMIP3) multimodel data set [*Meehl et al.* 2007]. Models (8 of the 25) that do not provide ice motion fields are not included. These models were discussed in the Intergovernmental Panel on Climate (IPCC) Change Fourth Assessment Report (IPCC-AR4; see *IPCC* [2007]). The model output used in this study is available through the Program for Climate Model Diagnosis and Intercomparison (PCMDI). Most models have more than one ensemble member, and we analyze only a single realization (ensemble member) from each model. Except for total sea ice extent, we examine observed thickness and motion fields that are within the Arctic Ocean domain shown in Figure 1a; it is that area bounded by the gateways into the Pacific (Bering Strait), the Canadian Archipelago and the Greenland (Fram Strait) and Barents Seas. All model fields are first projected onto a common grid (on a polar stereographic projection) prior to comparative analysis.

[6] In this study, we use model fields from 1979 to 1999 for the 20th century. Climate forcings applied over the 20th century differ for each model but are typically based on observational data sets. For the 21st century, we use 10 years (2000–2008) of output that is forced with the Special Report on Emission Scenarios (SRES) A1B "business as usual" scenario, where CO2 is projected to reach 720 ppm by 2100 (compared to ~370 ppm in 2000).

2.2. Sea Ice and Analyzed Meteorological Fields

[7] The gridded Arctic Ocean data sets used in this work include the: (1) daily fields of sea ice motion (SIM) and ice concentration from satellite passive microwave data (1979–2008); (2) time series of Fram Strait ice area export (IAE) from 1979 to 2008; (3) winter ice thickness from ICESat (2004–2008) [*Kwok et al.*, 2009]; and (4) sea level pressure (SLP) fields from NCEP/NCAR analysis. Passive microwave ice motion fields are those described by *Kwok et al.* [1998] and *Kwok* [2008]. Satellite passive microwave ice concentrations are from the Bootstrap algorithm. The time series of Fram Strait area export is estimated using passive microwave ice motion as described by *Kwok* [2009].

3. Taylor Diagrams

[8] In addition to the spatial fields shown in this paper, Taylor diagrams [*Taylor*, 2001] are used to summarize the scatter of the CMIP3 model fields (m) when compared with observations (o). We first provide a brief description of these diagrams before proceeding to the discussions of model scatter when compared to observations.

[9] These diagrams are useful for providing concise summaries of the relative merits of an ensemble of models: a single point on a two-dimensional (2-D) plot indicates the correlation coefficient (R), the root mean square difference between two fields (E^2), and the standard deviations of the model and observation patterns (σ_o, σ_m). As illustrated in Figure 1b, these four statistical quantities are related geometrically through the law of cosines. When normalized by the standard deviation of one of the fields (σ_o), the squared difference can be written as:

$$\hat{E}^2 = \left(\frac{E}{\sigma_o}\right)^2 = \hat{\sigma}_m^2 + 1 - 2R\hat{\sigma}_m; \qquad \hat{\sigma}_m = \frac{\sigma_m}{\sigma_o},$$

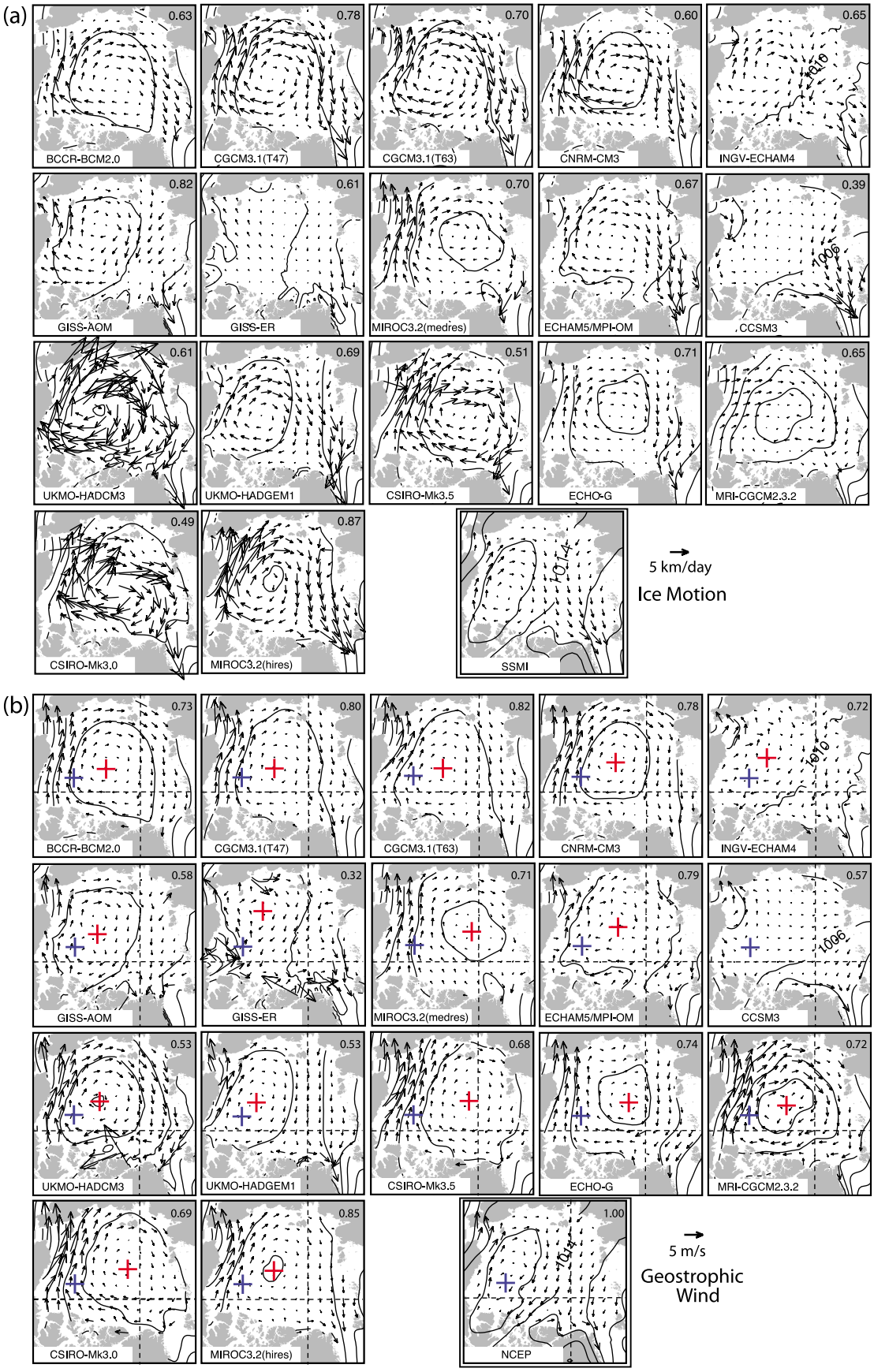
(a)
0.63
BCCR-BCM2.0
0.78
CGCM3.1(T47)
0.70
CGCM3.1(T63)
0.60
CNRM-CM3
0.65
INGV-ECHAM4
0.82
GISS-AOM
0.61
GISS-ER
0.70
MIROC3.2(medres)
0.67
ECHAM5/MPI-OM
0.39
CCSM3
0.61
UKMO-HADCM3
0.69
UKMO-HADGEM1
0.51
CSIRO-Mk3.5
0.71
ECHO-G
0.65
MRI-CGCM2.3.2
0.49
CSIRO-Mk3.0
0.87
MIROC3.2(hires)
SSMI
5 km/day
Ice Motion
(b)
0.73
BCCR-BCM2.0
0.80
CGCM3.1(T47)
0.82
CGCM3.1(T63)
0.78
CNRM-CM3
0.72
INGV-ECHAM4
0.58
GISS-AOM
0.32
GISS-ER
0.71
MIROC3.2(medres)
0.79
ECHAM5/MPI-OM
0.57
CCSM3
0.53
UKMO-HADCM3
0.53
UKMO-HADGEM1
0.68
CSIRO-Mk3.5
0.74
ECHO-G
0.72
MRI-CGCM2.3.2
0.69
CSIRO-Mk3.0
0.85
MIROC3.2(hires)
1.00
NCEP
5 m/s
Geostrophic
Wind

Figure 2

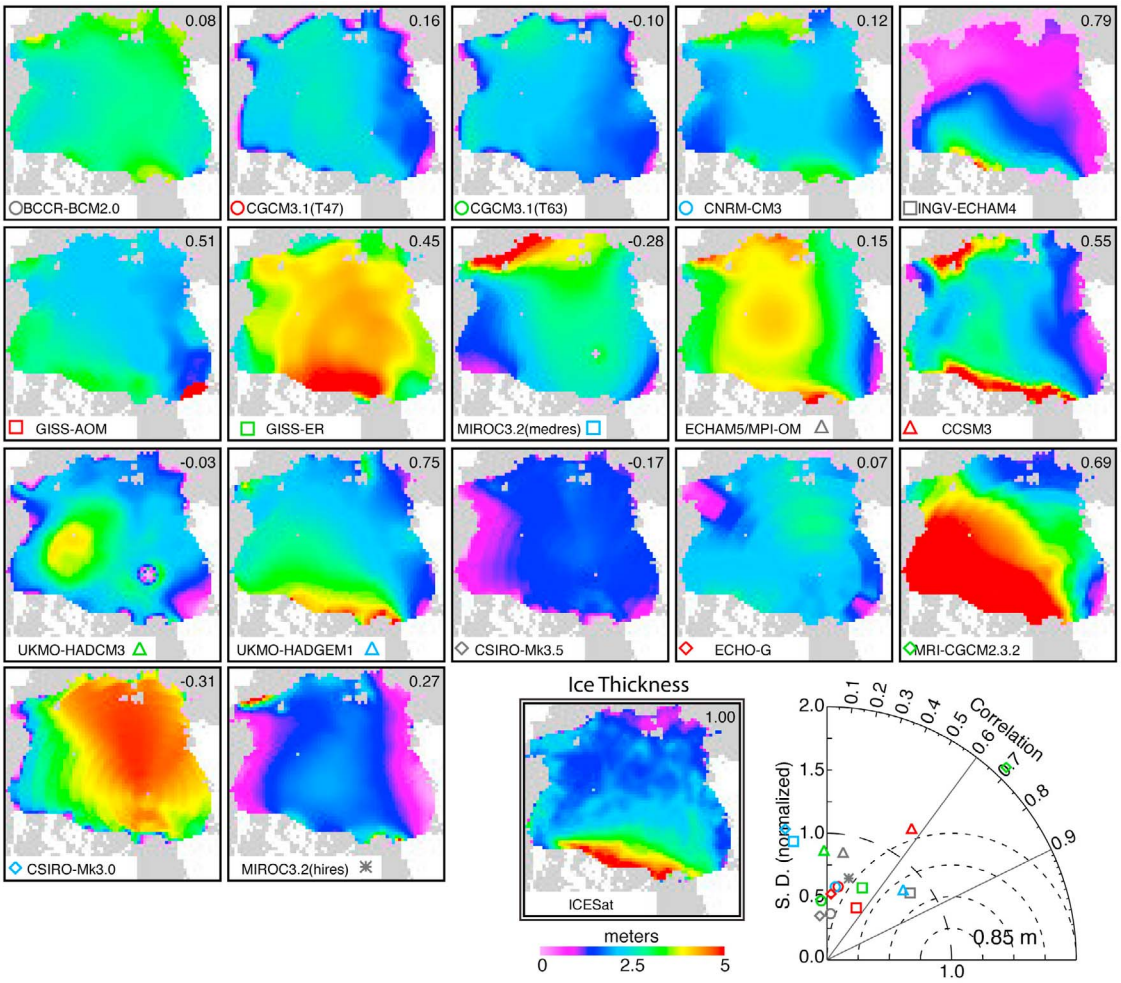

Figure 3. Mean winter Arctic sea ice thickness (2004–2008) of the 17 CMIP3 models compared with estimates from ICESat. Taylor diagram summarizes the pattern statistics (correlation and RMS differences). CMIP3 model identifiers are shown at the bottom of each field.

where

$$R = \frac{1}{\sigma_m \sigma_o \cdot N} \sum_{n=1}^{N} (f_n - \bar{f})(r_n - \bar{r}).$$

[10] In this normalized form of the Taylor diagram, the polar coordinates $\hat{\sigma}_m$ and $\cos^{-1}R$ specify the location of each point on the plot. The base of the triangle in Figure 1b is always unity (i.e., $\sigma_m = \sigma_o$). In the following discussions, the subscripts m and o refer to the model-simulated and observed fields, respectively. In each diagram (see Figure 1b), the dashed semicircles centered at unity on the abscissa are measures of the normalized distance ($\hat{E}$) between the reference and observed fields, as described in the above equation. Each point on the plot describes how closely the model-simulated field resembles the observed field on the basis of the three normalized statistical measures (i.e., $\hat{E}$, $\frac{\sigma_m}{\sigma_o}$, R) discussed above. Henceforth, we refer to these normalized measures as the "pattern statistics" (PS) of a given spatial and/or temporal pattern when compared with observations.

4. Analysis

[11] The comparisons between model and data are shown in Figures 2, 3, 4, and 5. Figures 2 and 3 contrast the mean spatial fields of ice motion, SLP, geostrophic wind and thickness. Figure 4 summarizes the pattern statistics, in Taylor diagrams, of the climatologies of annual cycles and mean patterns of ice motion, SLP, and geostrophic wind. These climatologies are constructed from averages of the monthly/annual fields between 1979 and 2008. Geostrophic wind (GW) is computed from SLP fields. Since it is not expected that these climate models reproduce a particular observed

Figure 2. Mean ice motion, sea level pressure, and geostrophic wind fields of the 17 CMIP3 models compared with those from satellite and analyzed NCEP/NCAR fields. Correlation coefficients are shown on the top right-hand corner of each field. The observed center of the Beaufort High (blue crosses) is compared to the location of the center (red crosses) in each model. CMIP3 model identifiers are shown at the bottom of each field. (Contour interval is 1.5 hPa.)

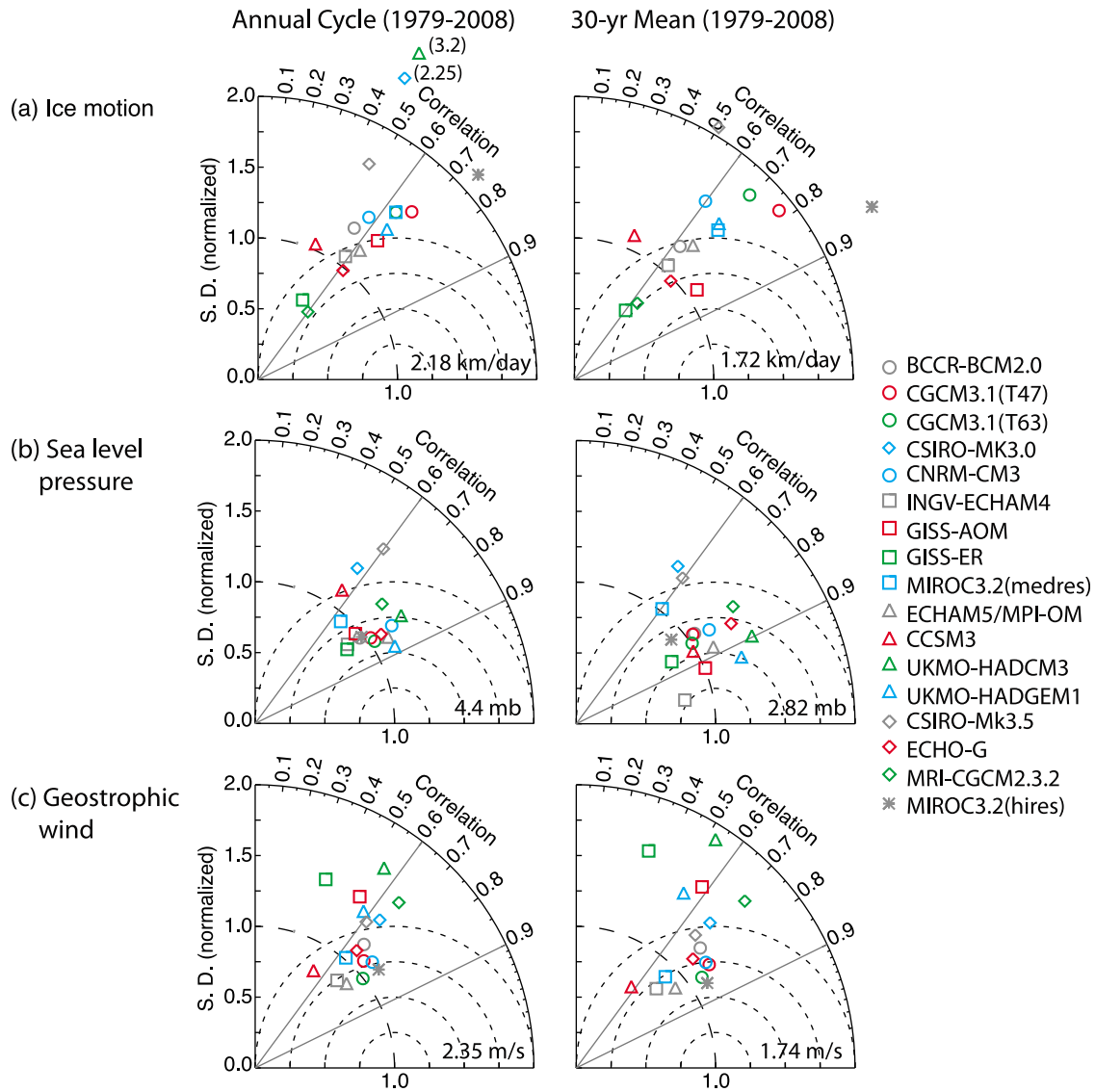

Figure 4. Comparison the 17 CMIP3 model and observed fields summarized in Taylor diagrams: (a) sea ice motion, (b) sea level pressure, and (c) geostrophic wind. The pattern statistics are relative to their annual cycle and mean climatologies (1979–2008). The standard deviation of the reference field (σ_o) is shown on the bottom right-hand corner of each diagram. CMIP3 model identifiers are shown at right.

time evolution of a given parameter, there is no assessment of time correlation. However, we do expect these uninitialized climate models to be able to simulate the spatial distribution of the mean climate, and the spatial and temporal distribution of the annual cycle. Thus, the focus of this analysis is on the annual cycles and the mean patterns.

[12] The Taylor diagrams in Figure 4 are organized a follows. There are two diagrams for each of the spatial fields (SIM, SLP, and GW): the fields of the annual cycle and the 29 year mean from the last 20 years of the 20th century, and the first 9 years of the 21st century. The standard deviation of the observed or reference field, σ_o, is shown on the bottom right-hand corner of each diagram. Comparisons of the PS provide assessments of the variability of annual cycles and the mean patterns.

[13] Separately, we examine the PS of the mean sea ice thickness distribution in the Arctic Ocean (in Figure 3) because of limited time span (2004–2008) of the ICESat data. Since the spatial pattern of sea ice coverage varies slowly and represents an integrated response to polar climate, we believe that this assessment is valid even though the observational record is short. Comparisons with the monthly and annual climatologies of Fram Strait IAE and average September sea ice extent are shown in Figure 5. We note that the model outputs are examined as an ensemble, and we make no attempts to explore the relative merits of each model.

4.1. Sea Ice Motion and Fram Strait Ice Export

[14] Following *Thorndike and Colony* [1982], we treat the two components of the SIM vectors as the real and imaginary parts of complex numbers in the computation of variance and correlation. The resulting correlation and variances of

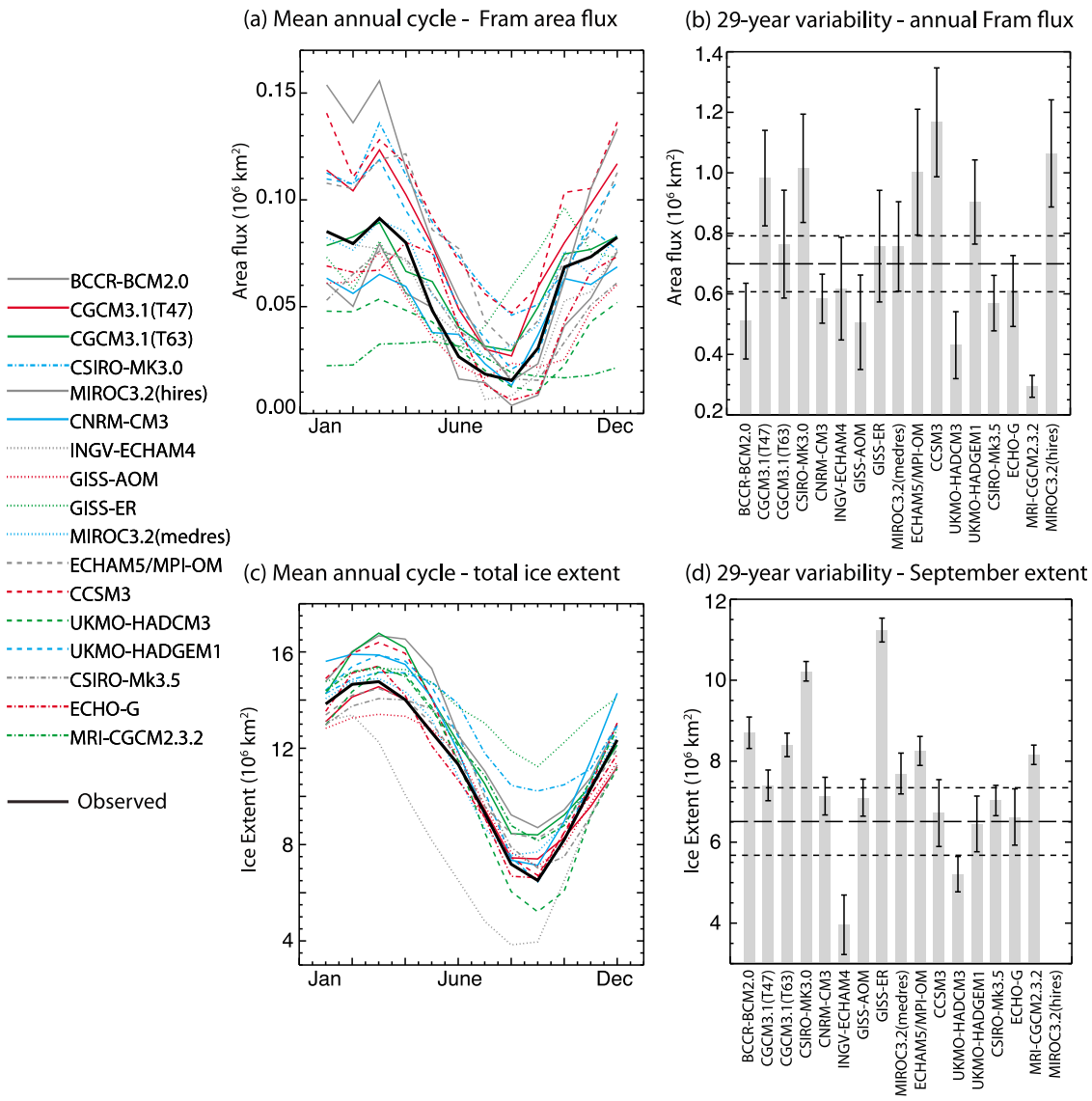

Figure 5. Comparison with climatologies (1979–2008) of Fram Strait area outflow and sea ice extent: (a and b) annual cycle and 29 year mean/variance of Fram Strait area flux, (c) annual cycle of Arctic ice extent, and (d) September ice extent. Dashed lines in Figures 5b and 5d represent mean and standard deviation of the observed quantity. MIRO3.2(hires) does not report ice extent.

the two complex fields are real numbers that are plotted on a Taylor diagram.

[15] Figure 2a contrasts the 29 year mean sea ice motion fields from observations (bottom right) with those from models. It can be seen that, while the characteristic anticyclonic (clockwise) motion of sea ice is seen in all the models, there is a broad scatter in the strength and the location of the center of the circulation pattern. It seems apparent from the spatial pattern of the SLP isobars the atmospheric forcing patterns are displaced from its expected location in the southern Beaufort. We return to the discussion of this arrangement of the SLP patterns when we examine the GW fields.

[16] The Taylor diagrams in Figure 4a summarize the distribution of PS in the annual cycle and mean climatologies of sea ice motion. The distances ($\hat{E}$) of individual model fields from the observed fields, and intermodel scatter are large. Some models tend to exaggerate and some tend to grossly underestimate the variability relative to the observed fields. This can be seen in the radial distribution of PS in the Taylor diagram (Figure 4a). Correlations of the annual cycles are consistently less than 0.7, the normalized standard deviations $\hat{\sigma}_m$ $(= \sigma_m/\sigma_o)$, ranges from 0.4 to greater than 3.2. Correlations of the mean fields are somewhat higher as evidenced by a clockwise rotation of the ensemble of PS; also, the range of $\hat{\sigma}_m$ is reduced. In general, the correlations are all less than 0.6. These results indicate also that, in a majority of the models, the large-scale average circulation of sea ice in the Arctic is roughly reproduced when compared to the observed annual cycle and mean patterns.

[17] Fram Strait IAE is the integral of the product between the gate-perpendicular component of the SIM and ice concentration along the ~400 km fluxgate between Greenland and Svalbard (shown in Figure 1a). Comparison of the annual

cycle and the mean pattern of the 17 models with those from observations are shown in Figures 5a and 5b. Even though there is an annual cycle in all the models (Figure 5a), their strength or amplitude vary significantly; their month-to-month intermodel scatter is also high. This scatter is large during the winter months when the area export is expected to be the highest owing to the annual pattern in SLP. In January, the intermodel scatter ranges from ~0.25 to 1.8 times the observed mean IAE. Mean and variance of the model and observed IAE over the 29 year period are contrasted in Figure 5b. As with the annual cycles, the intermodel scatter is large and thus deviations from the observed mean in ice flux.

[18] The IAE at Fram Strait may be modeled poorly since the persistent outflow of sea ice is dependent on the correct simulation of the strength and pattern of sea ice circulation within the Arctic Basin. If the orientation of the TDS (an important feature in the circulation field) within the Arctic Basin is shifted, then the magnitude and direction of sea ice export into the Greenland Sea could be significantly different from that observed. This is certainly suggested by the spatial patterns as well as PS of the motion fields discussed above.

4.2. Mean September Ice Extent

[19] Sea ice extent (SIE) is the sum of the area of grid cells with at least 15% ice concentration. The seasonal cycles of SIE are contrasted in Figure 5d. Except for three models, behavior of the models seem to be more clustered compared to that exhibited by the Fram Strait IAE. The modeled average September ice extent over the period 1979–2008, a parameter of community interest, is generally higher than that observed. This is not so surprising since few models exhibit negative trends and variability that are comparable to observations during the first 10 years of the 21st century [*Stroeve et al.*, 2007].

4.3. Sea Ice Thickness

[20] Model ice thickness is compared with an ice thickness field that is the average of the thickness estimates from five winter ICESat campaigns (2004–2008) [*Kwok et al.*, 2009]. Each campaign covers a ~33 day period between approximately mid-February and mid-March. The mean spatial patterns of ice thickness are shown in Figure 3. Similar to above, the PS (also in Figure 3) show large model-data differences and intermodel scatter.

[21] Ten of the 17 models have correlations <0.2 with several having negative correlations. Of the remaining seven, there are only three with correlations >0.6. Spatial variability is generally lower than observed. These correlations measure the similarities in the model and observed spatial distributions of ice thickness in the Arctic Basin. The spatial pattern of ice thickness over the Arctic, with thicker ice off the north margins of Greenland and the Canadian Arctic Archipelago and thinner seasonal ice north of Alaska and the Siberian Coast, can be considered a climatic feature. This feature was first observed in submarine ice draft in the 1950s and recently in satellite altimetry. It is a consequence of and maintained by the large-scale atmosphere/ocean forcing, and the dynamics (ice circulation and ice export) and thermodynamics (growth and melt) of the Arctic Ocean sea ice cover. This distribution of thickness can be seen in the average ICESat field in the bottom right of Figure 3. We find this large-scale climatic feature, the thickest ice on the correct side of the basin, in only a handful of model fields. In several models, thick ice is found in the wrong parts of the Arctic.

4.4. Sea Level Pressure and Geostrophic Wind

[22] The spatial distributions of SLP are especially interesting because the horizontal gradient of these scalar fields (wind) is the primary driver of sea ice circulation and ice export at Fram Strait, which in turn determines the spatial pattern of Arctic ice thickness. Thus, the character of the sea ice cover as described by variables examined above (ice motion, export, and thickness, perhaps to a lesser degree ice extent) is dependent on the accurate simulation of the spatial pattern of SLP distribution.

[23] Figure 2b compares the spatial fields of model and analyzed SLP and GW, and Figures 4b and 4c show the PS of the annual cycles and mean patterns same fields. It is striking to see, considering the intermodel scatter seen in the normalized PS of the ice motion fields (seen in Figure 4a), that the SLP and GW PS are more clustered (Figures 4b and 4c). Correlations are better than 0.55. Compared to the climatologies from the observed fields, the PS (correlation and intermodel scatter) of the GW are poorer than the PS of SLP. Overall correlations are reduced and intermodel scatter is increased. Gradients in the SLP highlight differences in the potential field. The large intermodel scatter in the SIM compared to the more moderate scatter in GW is possibly an indication of the differences in how the wind forcing is translated into ice velocity through the ice dynamics code in individual models.

[24] It is also evident that the centers of the pattern of high pressure in the model fields (as indicated by the red cross in Figure 2b) are significantly shifted toward the center of the Arctic Ocean compared to its observed mean location over the southern Beaufort Sea (as indicated by the blue crosses). This changes the circulation and spatial distribution of ice thickness throughout the basin. In the Arctic, the large-scale mean circulation of sea ice (see Figure 2b) is dominated on average by an anticyclonic (clockwise) pattern (Beaufort Gyre) in the western Arctic driven by a mean high-pressure pattern centered over the Beaufort Sea. The TDS that is associated with the strength of the low in the eastern Arctic. These results suggest that the correct geographic location, not only their relative locations, of these patterns of highs and lows are of primary importance (from a sea ice perspective) in improving the model-data agreement in terms of sea ice circulation, and distribution and ice export. These patterns are of significance in the sea ice and freshwater balance of the Arctic Ocean.

5. Conclusions

[25] In this paper, we compared the CMIP3 model output with observations of sea ice motion, export, extent, and thickness, and analyzed fields of sea level pressure and geostrophic wind of the Arctic Ocean at different averaging time scales. These variables play important roles in the distribution and annual balance of the sea ice mass within the Arctic basin. The aim is to examine the similarity of the simulations to observed and analyzed fields of the Arctic.

The models are examined as a group with no attempts made to explore the relative merits of individual models within the ensemble. There is a distribution in model performance in the collection, but some are clearly better than other. These assessments serve to summarize ensemble behavior, as baselines for measuring improvements, and as measures of reliability of CMIP3 output (and perhaps CMIP5 model fields) for projection of realistic decline rates of Arctic sea ice coverage.

[26] In examination of the pattern statistics and comparative variability, the skill of the CMIP3 models (as a group) in simulation of observed Arctic sea ice motion, Fram Strait export, extent, and thickness between 1979 and 2008 seems rather poor. Model-data differences and intermodel scatter of the sea ice parameters in the summarizing statistics are high. The spatial pattern of Arctic sea ice thickness, a large-scale slowly varying climatic feature of the ice cover, is not reproduced in a majority of the models. We attribute this in part to the pattern of atmospheric forcing (SLP fields) of ice motion, and export in the models. Misplacement of the large-scale mean features of the circulation pattern (the Beaufort Gyre and Transpolar Drift Stream) introduces large differences in Arctic sea ice motion, export, and thickness, and thus basin-scale sea ice mass balance. As seen in the model fields, the mean high-pressure pattern in the southern Beaufort is significantly displaced toward the central Arctic Basin from its expected location in a majority of models.

[27] Arguably one of the most important connections between the Arctic and global climate is through the Arctic Oscillation (AO) pattern in hemispheric SLP. *Rigor et al.* [2002] have shown distinctive anomalies of ice extent, ice advection, and surface temperature associated with the strength/polarity of the AO index. The signature of the AO on Arctic Ocean SLP is offset toward Siberia so that when AO is positive, the resulting combined dipole pattern accelerates the Transpolar Drift locally and shifts the circulation in the basin. This is not possible in the models if the mean high pattern is centered over the basin. Consequently the models will not get the main features of natural sea ice variability that may be dominating recent SIE declines as well as the long-term greenhouse response.

[28] While it is not expected that these uninitialized models agree completely with observations, especially at shorter time scales, the ice circulation, export, and thickness are nevertheless of importance at these time scales if reliable projections of the expected decline rates of the Arctic sea ice coverage are of interest. Because the model simulations have difficulties reproducing the mean patterns of Arctic circulation and thickness, our assessment suggests considerable uncertainties in the projected rates of sea ice decline even though the CMIP3 data set agrees that increased greenhouse gas concentrations will result in a reduction of Arctic sea ice area and volume. We anticipate that the climatologies shown here and this type of analysis shown will be potentially useful for evaluation of CMIP5 model output, which will include decadal hindcasts and predictions of sea ice behavior.

[29] **Acknowledgments.** I wish to thank G. F. Cunningham and S. S. Pang for their software support. We acknowledge the modeling groups, the PCMDI, and the WCRP's Working Group on Coupled Modeling for their roles in making available the WCRP CMIP3 multimodel data set. Support of this data set is provided by the Office of Science, U.S. Department of Energy. The SMMR and SSM/I brightness temperature and ice concentration fields are provided by the World Data Center A for Glaciology/National Snow and Ice Data Center, University of Colorado, Boulder, Colorado. This work was performed at the Jet Propulsion Laboratory, California Institute of Technology, under contract with NASA.

References

Eisenman, I., N. Untersteiner, and J. S. Wettlaufer (2007), On the reliability of simulated Arctic sea ice in global climate models, *Geophys. Res. Lett.*, *34*, L10501, doi:10.1029/2007GL029914.

Hassol, S. J. (2004), *Impacts of a Warming Arctic*, Arct. Clim. Impact Assess., Cambridge Univ. Press, Cambridge, U. K.

Holland, M. M., M. C. Serreze, and J. Stroeve (2010), The sea ice mass budget of the Arctic and its future change as simulated by coupled climate models, *Clim. Dyn.*, *34*, 185–200, doi:10.1007/s00382-008-0493-4.

Intergovernmental Panel on Climate Change (IPCC) (2007), *Climate Change 2007: The Physical Science Basis: Contribution of Working Group I to the Fourth Assessment Report of the IPCC*, edited by S. Solomon et al., Cambridge Univ. Press, New York.

Kwok, R. (2008), Summer sea ice motion from the 18 GHz channel of AMSR-E and the exchange of sea ice between the Pacific and Atlantic sectors, *Geophys. Res. Lett.*, *35*, L03504, doi:10.1029/2007GL032692.

Kwok, R. (2009), Outflow of Arctic sea ice into the Greenland and Barents Seas: 1979–2007, *J. Clim.*, *22*, 2438–2457, doi:10.1175/2008JCLI2819.1.

Kwok, R., A. Schweiger, D. A. Rothrock, S. Pang, and C. Kottmeier (1998), Sea ice motion from satellite passive microwave data assessed with ERS SAR and buoy data, *J. Geophys. Res.*, *103*, 8191–8214, doi:10.1029/97JC03334.

Kwok, R., G. F. Cunningham, M. Wensnahan, I. Rigor, H. J. Zwally, and D. Yi (2009), Thinning and volume loss of the Arctic Ocean sea ice cover: 2003–2008, *J. Geophys. Res.*, *114*, C07005, doi:10.1029/2009JC005312.

Meehl, G. A., C. Covey, T. Delworth, M. Latif, B. McAvaney, J. F. B. Mitchell, R. J. Stouffer, and K. E. Taylor (2007), The WCRP CMIP3 multi-model dataset: A new era in climate change research, *Bull. Am. Meteorol. Soc.*, *88*, 1383–1394, doi:10.1175/BAMS-88-9-1383.

Rigor, I. G., J. M. Wallace, and R. L. Colony (2002), Response of sea ice to the Arctic Oscillation, *J. Clim.*, *15*, 2648–2663, doi:10.1175/1520-0442(2002)015<2648:ROSITT>2.0.CO;2.

Stroeve, J., M. M. Holland, W. Meier, T. Scambos, and M. Serreze (2007), Arctic sea ice decline: Faster than forecast, *Geophys. Res. Lett.*, *34*, L09501, doi:10.1029/2007GL029703.

Taylor, K. E. (2001), Summarizing multiple aspects of model performance in a single diagram, *J. Geophys. Res.*, *106*, 7183–7192, doi:10.1029/2000JD900719.

Thorndike, A. S., and R. Colony (1982), Sea ice motion in response to geostrophic winds, *J. Geophys. Res.*, *87*, 5845–5852, doi:10.1029/JC087iC08p05845.

Wang, M., and J. E. Overland (2009), A sea ice free summer Arctic within 30 years?, *Geophys. Res. Lett.*, *36*, L07502, doi:10.1029/2009GL037820.

Zhang, X., and J. E. Walsh (2006), Toward a seasonally ice-covered Arctic Ocean: Scenarios from the IPCC AR4 model simulations, *J. Clim.*, *19*, 1730–1747, doi:10.1175/JCLI3767.1.

R. Kwok, Jet Propulsion Laboratory, California Institute of Technology, Mail Stop 300-331, 4800 Oak Grove Dr., Pasadena, CA 91109, USA. (ron.kwok@jpl.nasa.gov)